



**HAL**  
open science

# Imaging grain boundary grooves in hard-sphere colloidal bicrystals

Éric Maire, Emily Redston, Maria Persson Gulda, David A Weitz, Frans Spaepen

► **To cite this version:**

Éric Maire, Emily Redston, Maria Persson Gulda, David A Weitz, Frans Spaepen. Imaging grain boundary grooves in hard-sphere colloidal bicrystals. *Physical Review E*, 2016, 94 (5), pp.059902. 10.1103/PhysRevE.94.059902 . hal-01538194

**HAL Id: hal-01538194**

**<https://hal.science/hal-01538194>**

Submitted on 9 Feb 2022

**HAL** is a multi-disciplinary open access archive for the deposit and dissemination of scientific research documents, whether they are published or not. The documents may come from teaching and research institutions in France or abroad, or from public or private research centers.

L'archive ouverte pluridisciplinaire **HAL**, est destinée au dépôt et à la diffusion de documents scientifiques de niveau recherche, publiés ou non, émanant des établissements d'enseignement et de recherche français ou étrangers, des laboratoires publics ou privés.

# Imaging Grain Boundary Grooves in Hard–Sphere Colloidal Bi-crystals

Eric Maire,<sup>1,2</sup> Emily Redston,<sup>3</sup> Maria Persson Gulda,<sup>1</sup> David Weitz,<sup>1,4</sup> and Frans Spaepen<sup>1</sup>

<sup>1</sup>*Harvard University, School of Engineering and Applied Science, Cambridge, MA 02138*

<sup>2</sup>*Now at Laboratoire Matériaux, Ingénierie et  
Sciences (MATEIS) INSA-Lyon / UMR CNRS 5510,  
25 avenue Jean Capelle, F-69621 Villeurbanne, France\**

<sup>3</sup>*Harvard University, School of Engineering and Applied Sciences, Cambridge, MA 02138*

<sup>4</sup>*Harvard University, Physics Department,  
Cambridge, Massachusetts 02138, USA*

(Dated: August 23, 2016)

## Abstract

Colloidal particles were sedimented onto patterned glass slides to grow three-dimensional bi-crystals with a controlled structure. Three types of symmetric tilt grain boundaries between close-packed face-centered cubic crystals were produced:  $\Sigma 5$  (100),  $\Sigma 17$  (100) and  $\Sigma 3$  (110). The structure of the crystals and their defects were visualized by confocal microscopy, and characterized by simple geometric measurements, including image difference, thresholding and re-projection. This provided a quick and straightforward way to detect the regions in which the atoms are mobile. This atomic mobility was higher at the grain boundaries and close to the solid/liquid interface. This method was compared to the more conventional analysis based on the calculation of the local order parameter of the individual particles to identify the interface. This was in turn used to identify the presence of grooves at the grain boundary / liquid triple junction for every type of grain boundary, except for the twin ( $\Sigma 3$  (110)), for which no groove could be detected. Images of these grooves were processed and the angle linking the grain boundary energy to the solid/liquid interfacial energy was measured. The resulting values of the grain boundary energy were compared to estimates based on the density deficit in the boundary.

Keywords: colloids, grain boundaries

---

\* eric.maire@insa-lyon.fr

## I. INTRODUCTION

Colloidal systems provide unique opportunities to study the dynamics of crystals and glasses. Colloidal particles with a diameter on the order of a micrometer can be observed in the optical microscope. In particular, confocal microscopy offers the opportunity to track the particles in time and space and thereby provides a direct particle-level view of a variety of complex phenomena such as the nucleation and growth of crystal nuclei in a metastable liquid [1], the nucleation of liquids in overheated crystals [2], the capillary fluctuations of a crystal-liquid interface [3], the nucleation and growth of misfit dislocations in a crystal grown epitaxially on a patterned template [4], the nucleation of dislocations under an indenter tip [5] and the local transformations during the shear deformation of a glass [6, 7].

Grain boundaries, which we will take here to be the boundaries between two identical crystals with a different orientation, have a complex structure [8, 9]: five angles are required for a full macroscopic identification (three for the relative orientation of the crystals, two for the orientation of the boundary plane). Microscopically, they consist of interlocking steps on the surfaces of the grains they bound. Often they are faceted and contain defects, such as grain boundary dislocations. Their dynamics, such as atomic diffusion along them, or atoms detaching themselves from one grain and joining to the other causing boundary motion, are key to the understanding of phase transformations, high-temperature deformation and grain growth.

The static structure of grain boundaries can, with some effort, be elucidated by electron microscopy, but a direct view of their atomic-level dynamics remains beyond reach. This is where colloidal modeling offers a unique opportunity. Most of the work so far has been on boundary lines between two-dimensional crystals, such as the capillary fluctuation study by Skinner *et al.* [10]. Randomly oriented boundaries between three-dimensional colloidal crystals have been used to claim glassy dynamics [11], to study their kinetic roughening and grain growth [12], and investigate their role in the nucleation of melting [13]

We have proposed a method to produce grain boundaries between hard-sphere colloidal crystals with prescribed orientation, by sedimentation onto specially oriented bicrystal templates [14]. In this paper we introduce a method to investigate the energy of these grain boundaries by a new efficient way to image the triple lines they form with the crystal-liquid

interface.

The equilibrium configuration at a triple line where three interfaces meet should satisfy the equation [15, 16]:

$$\sum_{i=1}^3 \left( \hat{t}_i \gamma_i + \frac{\partial \gamma_i}{\partial \beta_i} (\hat{t}_i \times \hat{s}) \right) \quad (1)$$

where  $\hat{t}_i$  are the unit vectors perpendicular to the triple line in each of the three interfaces,  $\hat{s}$  is the unit vector along the triple line,  $\beta_i$  are the angles each interface makes with a fixed direction, and  $\gamma_i$  are the interfacial energies. The second term in the parentheses is a "torque term" that arises from crystallographic anisotropy. The configuration in our experiments is illustrated in Fig. 1: a vertical, symmetric tilt boundary in equilibrium with two identical solid-liquid interfaces. Due to the symmetry of this configuration, the torque terms are zero or cancel out, and hence the equilibrium condition reduces to a simple vector equilibrium at a "grain boundary groove":

$$\gamma_{GB} = 2\gamma_{SL} \cos\left(\frac{\alpha}{2}\right) \quad (2)$$

where  $\gamma_{GB}$  and  $\gamma_{SL}$  are the grain boundary and solid-liquid interfacial energies, respectively, and  $\alpha$  is the groove angle. The curvature of the solid-liquid interface is the result of gravity, which maintains a horizontal solid-liquid interface at infinity.

The only observations of grain boundary grooves in colloidal systems are those of Rogers and Ackerson [17], who used hard-sphere-like polymer particles with a diameter of  $0.5 \mu m$  to form polycrystals in equilibrium with a liquid in a gravitational field. They observed several grain boundary grooves, and the objective of their study was to measure the solid-liquid interfacial energy from the curvature of the solid-liquid interface due to the density gradient, in analogy to similar experiments on molecular systems in a temperature gradient [18]. Our interest, however, is in the grain boundaries themselves, specifically the energies of custom-made examples.

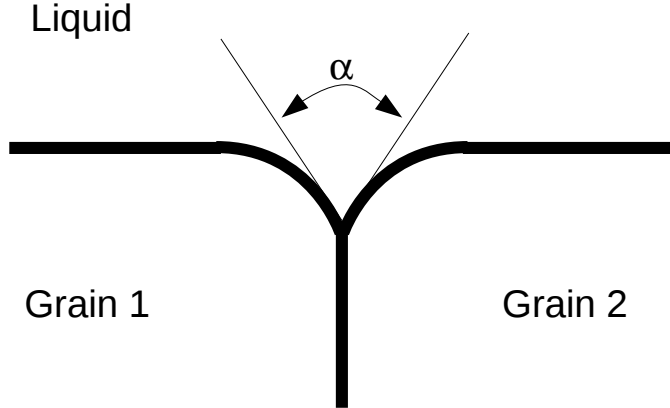


FIG. 1. Definition of the geometry of the groove at the grain boundary – liquid triple junction.

## II. EXPERIMENTAL METHODS

### A. Colloidal suspension

Silica particles (diameter  $\sigma = 1.55 \mu\text{m}$ , polydispersity  $< 3.5\%$ , density  $2.0 \text{ g/cm}^3$ , mass  $3.9 \times 10^{-15} \text{ kg}$ ) were suspended in a water - 62.8 vol.% dimethylsulfoxide (DMSO) solution that matched the index of refraction of the silica and had a density of  $1.1 \text{ g/cm}^3$ . Contrast between particles and liquid was achieved by adding 1.2 vol.% fluorescein–NaOH dye (3 wt.% in water) to the solution. The index match makes the system optically transparent, which allows investigation by optical confocal microscopy up to  $100 \mu\text{m}$  into the sample. The index match also minimizes the van der Waals forces between the particles, which interact therefore like hard spheres. The high concentration of electrolyte introduced with the fluorescein solution reduces the Debye screening length to 10 nm, consistent with hard-sphere interaction. The large difference in density,  $\Delta\rho$ , between the solution and the silica spheres results in a short gravitational length  $k_B T / \Delta\rho V_p g = \sigma/7$ , where  $V_p$  is the particle volume. As a result, the crystal-liquid interface that is formed after sedimentation is flat and well defined, but the liquid layer is only a few diameters thick [3].

## B. Template

The crystal growth is controlled by the use of a template. Hard spheres crystallize into close-packed structures: face-centered cubic, hexagonal close-packed, or random hexagonal close-packed. Spontaneous crystallization, for example by homogeneous nucleation [1], results in the formation of the latter structure, which consists of close-packed hexagonal planes stacked randomly in the A,B or C positions. To obtain large face-centered cubic crystals, as in this study, it is necessary to use templates [4, 19]. A template is a patterned substrate that directs the settling of the particles in such a way that the structure, orientation, and size of the crystal is pre-determined. This process, called colloidal epitaxy, is key to this study, in which we grow bi-crystals of specific orientation and symmetry.

### 1. Fabrication of the templates

A positive mask of the targeted pattern (set of holes) was printed on a chromium-coated substrate (chromium was removed using a Heidelberg<sup>TM</sup> mask maker). A thin layer of photoresist was spin-coated and polymerized (3 minutes at 110°C) on a primer-coated glass slide used as substrate. This assembly was then exposed using a mask aligner (Suss<sup>TM</sup>) for 2 to 2.5 sec. The exposure time depended on the size of the holes in the chromium mask, the age of the photoresist, calibration of the mask aligner and the premixed developer. The photoresist was then developed for 60 to 90 seconds. The silica was etched in a reactive ion etcher (RIE) for about 10 minutes. Finally, to remove the remaining photoresist, the sample was exposed in the same RIE to an oxygen cleaning plasma, which cleaned the photoresist without etching the silica.

### 2. Types of templates

The individual crystal patterns chosen to guide the growth of the colloidal face-centered cubic bi-crystals were similar to those presented in Refs [5, 19]. It was shown there that good crystal could grow on square lattices of holes spaced at 1.63  $\mu\text{m}$  pitch. This distance was selected because it corresponds to the observed inter-particle distance in crystals obtained by slow sedimentation on a flat, unpatterned glass slide. Crystals also form on a flat slide, but because of random simultaneous nucleation of differently oriented grains, the final structure

is a polycrystal with quasi-columnar grains. We have used some of these polycrystals for comparison in the present work.

The orientation of the crystal in the direction perpendicular to the substrate can be modified (engineered) by changing the geometry of the pattern, in order to impose a specific type of plane on the first layer, which in turn drives the orientation of the other layers parallel to the substrate. An hexagonal initial pattern, for instance, induces the successive growth of (111) closed-packed planes. This is also what spontaneously happens in the case of the polycrystals that form on a flat surface. A square pattern with a spacing of  $1.63 \mu\text{m}$  induces the growth of (100) planes. A rectangular pattern with a pitch of  $1.63 \mu\text{m}$  in one direction and of  $\sqrt{2} \times 1.63 \mu\text{m}$  in the perpendicular direction produces growth of (110) planes parallel to the substrate.

Three types of bi-crystalline patterns were generated to grow the following symmetric tilt boundaries: a  $\Sigma 5$  (100), a  $\Sigma 17$  (100), and a  $\Sigma 3$  (110). The patterns were taken from a catalogue of geometrically constructed hard-sphere boundaries [20–22]. The last one is a perfect twin boundary. These boundaries were selected because of their high degree of coincidence (low  $\Sigma$ ), and hence short repeat lengths. This was convenient for compatibility with the CAD software used to draw the template patterns. They are also some of the more widely used ones in computer simulation studies, and their energies are minima (cusps) in the orientation space [23–25].

Figure 2 shows a confocal image of each bicrystal, in a region close to the interface between the template and the colloidal suspension. The white dots in these figures are holes filled with the liquid. In some places, the bottom of some silica spheres can be seen inside the holes.

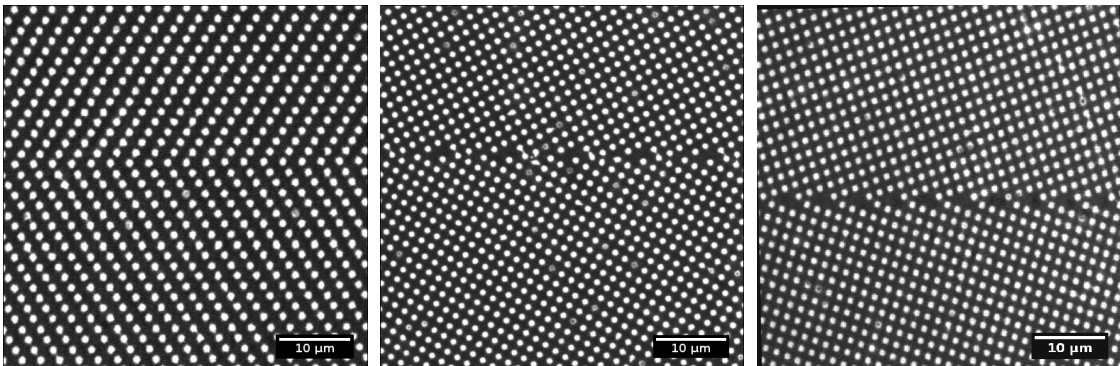


FIG. 2. Confocal images of the templates:  $\Sigma 3(110)$  (left),  $\Sigma 17(100)$  (middle) and  $\Sigma 5(100)$  (right).

## C. Confocal microscopy and processing of the images

### 1. Confocal microscopy

The structure of the bicrystals was observed with a Leica<sup>TM</sup> confocal microscope in resonant mode. The time required to image a sample was about 2 minutes. The magnification was set to obtain images with a  $0.1\ \mu\text{m}$  voxel size in the three dimensions of the analyzed volumes. Typical fields of view in the planes parallel to the substrates were  $51.2$  or  $102.4\ \mu\text{m}$  on a side. The size in the direction perpendicular to the template was governed by the height of the crystal, and was in the range of  $20$  to  $50\ \mu\text{m}$ . In order to reduce the noise in the image, each slice was averaged over four acquired frames. Since the refractive index of the fluid is matched to that of the spheres, light could penetrate deeply into the sample with little scattering, so that tens of crystal planes could be imaged. The lateral resolution (perpendicular to the optical axis) was about  $200\ \text{nm}$ , typical for optical microscopy. Because of the limitations of the optics, the vertical resolution was only  $500\ \text{nm}$ .

### 2. Image processing

A confocal image is a list of intensities (one value of the intensity for every pixel in the image). These intensities are coded using gray levels. In the present paper these gray levels vary from  $0$  (black) to  $255$  (white). The average gray levels of each slice were evened out and normalized to insure homogeneity from the top to the bottom of the sample. The normalized images were then median-filtered to reduce the noise and to facilitate the subsequent analysis.

There are a number of procedures to determine the numerical locations of the particle centers from the three-dimensional confocal images ("stacks") [26–28]. In this work, we have used a new, simple but practical method for this purpose, based on standard image processing techniques. First, a threshold was introduced to separate the silica phase (particles, dark) from the solution (light). The particles were then located by calculating the largest possible spheres that could be fit into the silica parts of the image. These spheres were gray-colored proportional to their radius. A new threshold was introduced to identify the largest spheres and reject the smaller, possibly interstitial, ones. The coordinates of the centers of the large spheres form the files for subsequent analysis.

We also developed an additional acquisition procedure, in which two consecutive images of the same volume at a given location were acquired, about two minutes apart, and the difference between the two images was computed. If the colloidal particles were perfectly immobile, these differences should be equal to zero. It will be shown that these differences are not zero, and that the locations where the difference is lower or higher than zero are places where the particles are mobile.

### III. PROCESSING THE IMAGES TO LOCATE THE SOLID/LIQUID INTERFACE

#### A. Standard procedure with a local order parameter

To distinguish the crystal and fluid phases, we assign an order parameter [29] to each particle based on the arrangement of its nearest neighbors. As in Ref.[3], we begin by finding the distance  $r_{ij}$  between a particle  $i$  and any other particle  $j$ . All particles with  $r_{ij}^2 < 1.45 \times r_0^2$  are considered nearest neighbors of particle  $i$ . The value  $r_0^2$  is found by identifying the six closest particles to  $i$  and calculating their mean squared separation

$$r_0^2 = \frac{1}{6} \sum_{j=1}^6 r_{ij}^2$$

Next we find the bond angles  $\theta_{jik}$  between any two neighbor pairs. The order parameter  $\phi_i$  is defined as the number of angles  $\theta_{jik} \approx 60^\circ$ . Since the experimental determination of the position of the centers of the particles is not perfect and their motion non-negligible, it is necessary to establish an angular tolerance for the determination of the order parameter ( $\cos \theta = 0.5 \pm 0.1$ ).

In an ideal face-centered cubic crystal the order parameter is 24. Point defects in the crystal lower the order parameter in their vicinity, and hence it is useful to determine an average value to aid in the identification of the interface. This is done by calculating the mean value for every particle  $i$  and its neighbors, defined as before. The local average  $\langle \phi_i \rangle$  is then assigned to the central particle  $i$ . Fig. 3 shows a typical snapshot of the boundary, colored according to the average order parameter. The crystal and liquid phases, along with the grain boundary, are clearly visible.

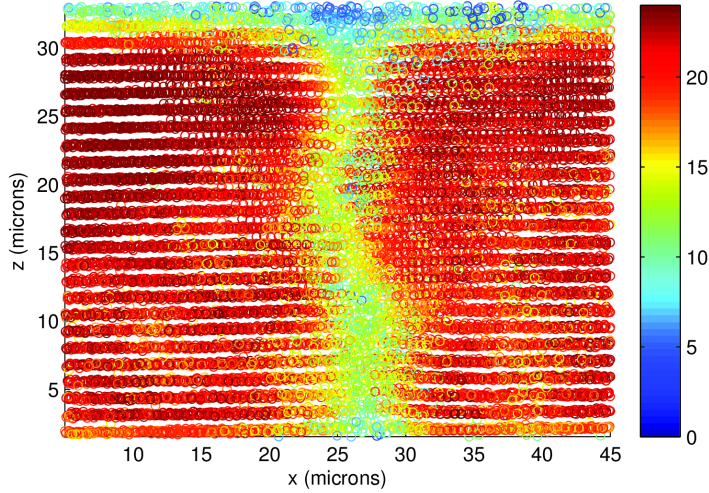


FIG. 3. Projection of the order parameter of all particles in the  $\Sigma 5$  (100) bicrystal. The grain boundary is perpendicular to the plane of the figure and the template is at the bottom. The color bar indicates the order parameter (0–24).

To image the groove at the triple line, we set a threshold value for the order parameter to define the interface between the solid and the liquid. Our system also has lower order parameters along the entire grain boundary, but we can get around this problem identifying the “liquid” particles as in Figure 4. This figure was created by coloring particles with an order parameter less than a threshold value white, and those above black. Each point was then broadened in the x- and z-directions by a Gaussian with a standard deviation of  $1.6 \mu\text{m}$ , and finally projected (averaged) in the y-direction. The resulting figure clearly shows the groove and the triple line.

### B. Particle mobility at the grain boundary

Fig. 5 shows the values of the gray scale differences between two consecutive confocal images of the same sample taken two minutes apart. Positive values are white and negative values are black; gray values are close to zero. Fig. 5(a) corresponds to a slice at the bottom of the sample while Fig. 5(b) is in the solid phase, but at a level close to the liquid. It can be



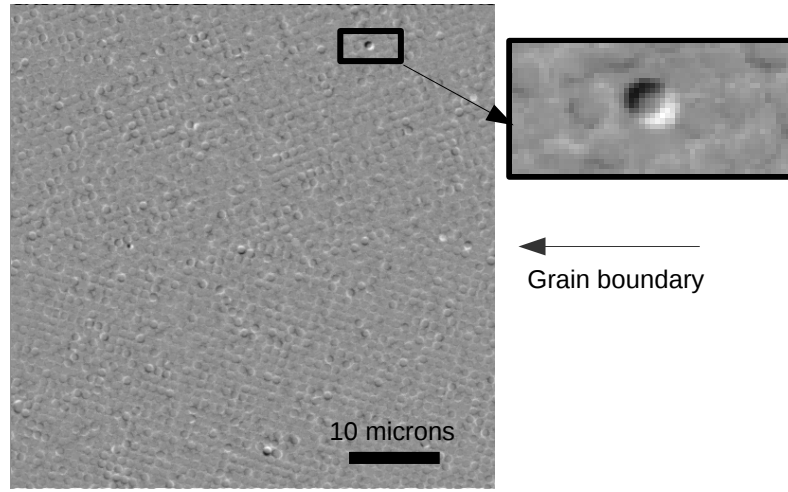
FIG. 4. Projection of particles with order parameters less than the threshold order parameter (11) in the  $\Sigma 5$  (100) bicrystal.

seen from these figures that the difference is not uniformly equal to zero. This is the result of Brownian motion. In most of the sample, this Brownian motion leads to small differences. In several places, however, the difference is greater and shows a characteristic black-and-white pattern. One such pattern is shown as a zoomed inset in Fig. 5(a). The difference has a high absolute value and goes from positive to negative. The difference plot highlights places where an atom has moved substantially between the two image acquisitions.

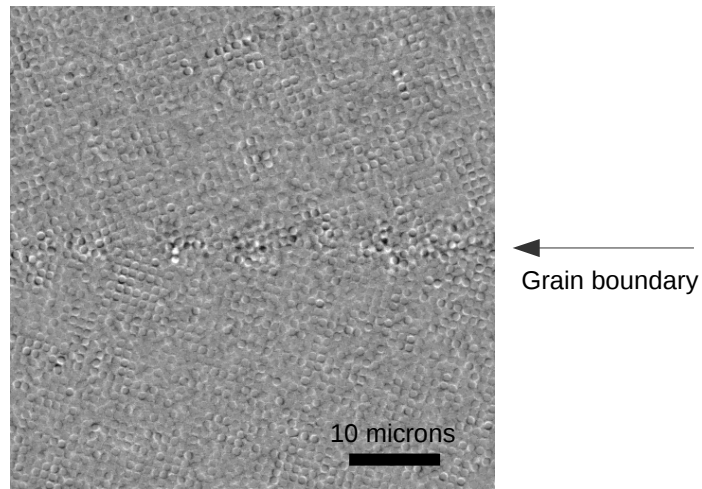
This effect can be seen in the bulk of a crystal (as in Fig. 5(a)), where it probably corresponds to vacancy motion. It is particularly prevalent at the grain boundary, where one would expect greater mobility of the particles due to the excess volume. We also expect it near the solid-liquid interface, where the liquid particles have greater mobility. This simple difference method, therefore, can be used to identify phases and locate the phase boundaries, as will be shown below.

### C. Visualizing the grooves with mobility

Images like the ones in Fig. 5 were first thresholded to select the regions in the sample where the difference is both very high (white gray levels) *and* very low (black gray levels).



(a)



(b)

FIG. 5. Difference between two consecutive confocal microscopy images of the same location taken two minutes apart. (a) Slice close to the template at the bottom of the sample and (b) Slice close to the liquid/solid interface. The grain boundary is horizontal in the middle of the images. Some particles have moved, leading to characteristic black and white patterns like the one shown as a zoomed inset in Fig. (a).

These binarized 3D images were then projected onto the plane perpendicular to both the grain boundary and the template. The result is shown in Fig. 6 which looks similar to the projected order parameter shown in Fig. 4. The figure shows two examples:  $\Sigma 5$  (100) (Fig.

6(a)) and a  $\Sigma 17$  (100) (Fig. 6(b)). This projected image of the mobility reveals the presence of a groove at the grain boundary – liquid triple line. This can only be observed if the grain boundary is carefully aligned with the three main axes of the confocal images. We have been able to reveal the presence of such grooves in all the grain boundaries that we have analyzed, with one exception: for the twin boundary ( $\Sigma 3$  (110)) Fig. 7), no groove can be observed. Since the twin boundary has zero excess volume, the mobility of its particles is no higher than that in the bulk crystal. Since in a hard-sphere system, the energy of a twin boundary is zero, Eq. (2) predicts that the groove angle is  $\alpha = 180^\circ$ , which means that there is no groove.

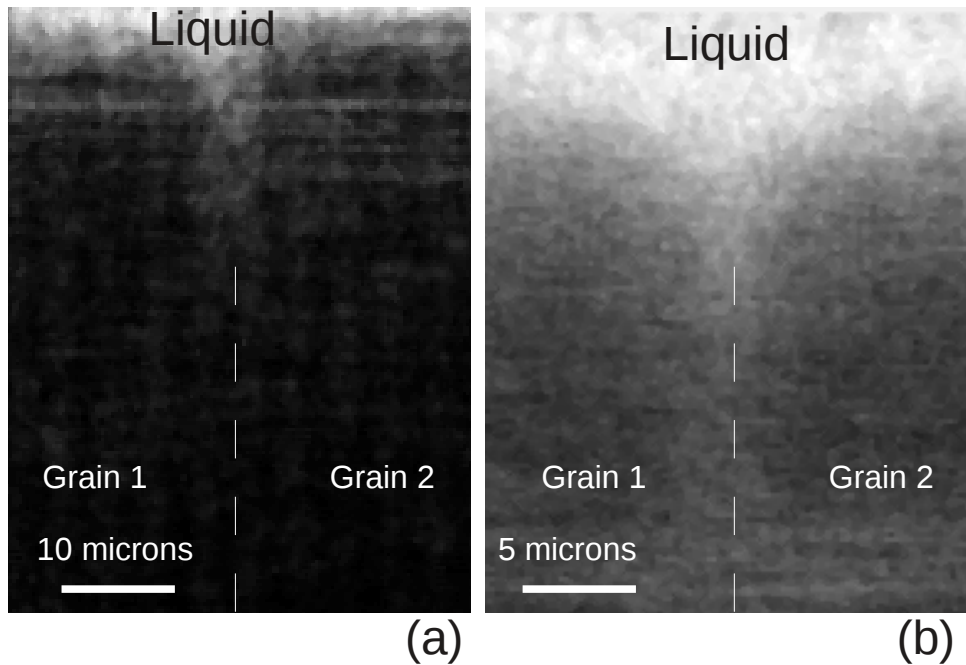


FIG. 6. Projected view of the mobility in a  $\Sigma 5$  (100) (a) and in a  $\Sigma 17$  (100) grain boundary (b). Grooves can be observed at the solid/liquid interface grain boundary tripple line.

Images like Fig. 6 can be processed further to retrieve a profile of the groove. This first requires a threshold of the projections, which has to be selected so that the liquid part of the sample is white and the solid is black. The value chosen for the threshold influences the results. The 2D images of the projections can then be analyzed to determine the local height of the solid/liquid interface. This value of the height, averaged along the total length

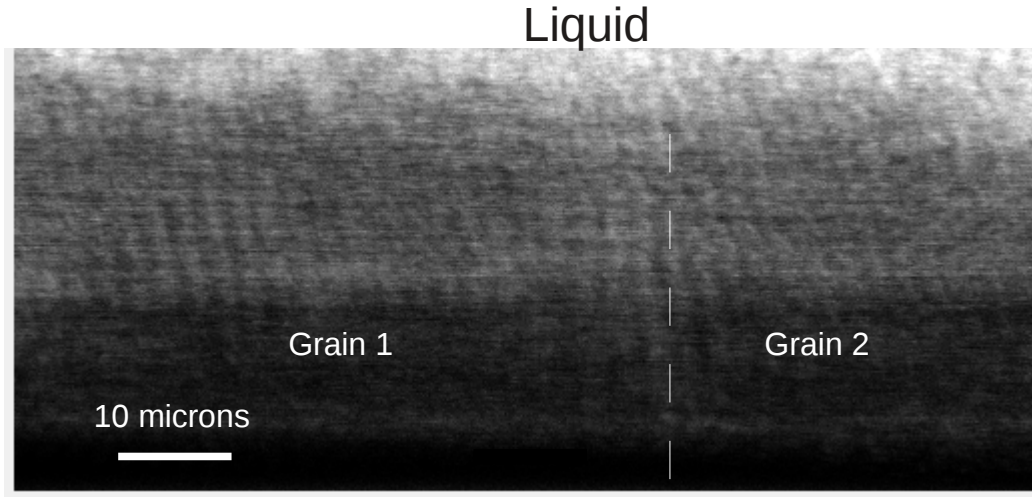


FIG. 7. Projected view of the mobility in a  $\Sigma 3$  (110) grain boundary. No groove can be observed.

of the boundary, defines the profile of the groove.

#### IV. COMPARISON BETWEEN THE TWO PROCESSING METHODS

The position of the interface determined using both the standard order parameter (OP) processing and the new image processing (IP) procedure presented in this paper both depend on the threshold to distinguish the solid and the liquid. Figure 8 shows the changes in the profile of the same groove when this threshold is changed for the two processing routes. Overlaid are the positions of the particles coloured according to their order parameter. Obviously, when the threshold increases, the position of the solid/liquid interface shifts up and the shape of the groove is also slightly modified. This is more pronounced with the IP than with the OP method. In the rest of the paper, we have used the same threshold value, IP 70, which gives a stable profile with a limited amount of noise. Figure 9 compares the two best choices: IP 70 and OP 11.

That the two interface profiles differ is no surprise, since the two methods are based on different physical principles: one is static, the other dynamic. At the level of the IP–

interface, the structure is not yet that of a liquid, but that of a crystal with lots of defects that allow mobility. For this reason, the IP–interface lies below the OP–interface. What is important, however, is that the groove shapes are similar and that the simple IP–technique can be used to determine groove angles.

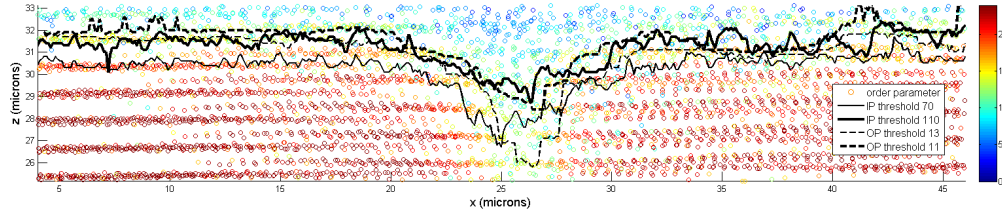


FIG. 8. Effect of the threshold used in the analysis of the position of the solid/liquid interface. The particles are coloured according to their order parameter and are also shown. Interface positions corresponding to different threshold values for the order parameter (OP) and for the image processing (IP) procedures are indicated.

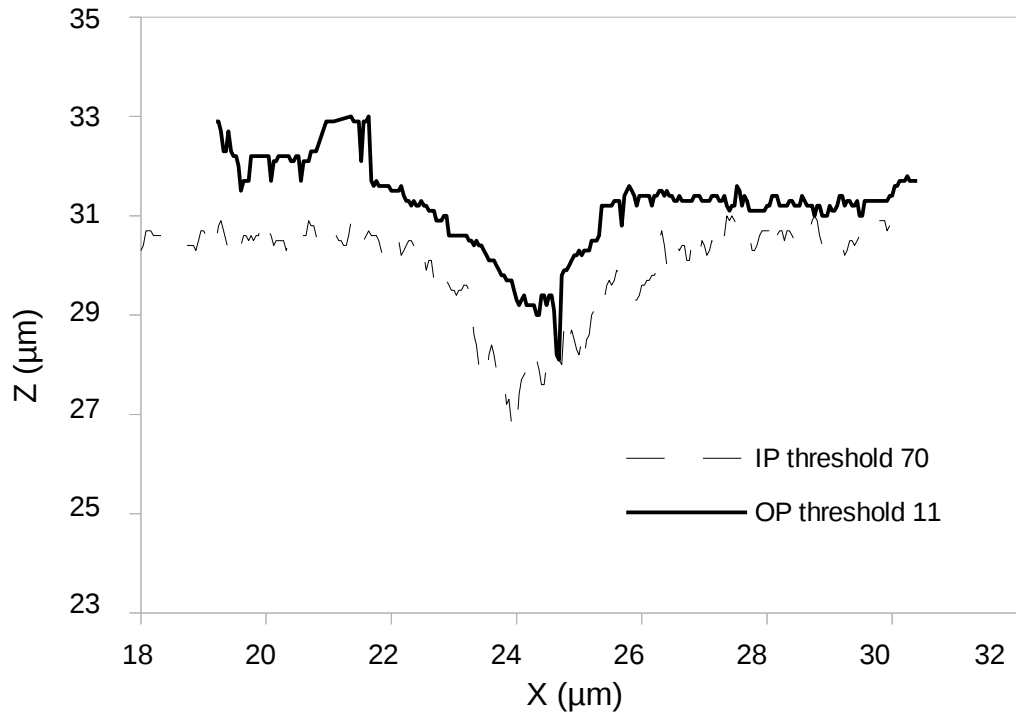


FIG. 9. Comparison of the two best thresholds using the order parameter (OP) and the image processing (IP) procedures.

## V. QUANTITATIVE RESULTS

### A. Profiles of the grooves

The groove profile can be fitted with a mathematical function. We chose two sine functions (one for each branch of the profile on each side of the grain boundary), but any function that fits the curve close to the triple line can be used. The effect of the choice of this function on the results is much smaller than that of other sources of uncertainty. Fig. 10 shows a typical fit. The slope of this function at the groove point then gives the two contributions of the angle  $\alpha$  (one on each side of the groove). Ideally, these two contributions should be equal and the grain boundary perfectly vertical. Experimentally, as seen in Figure 10 and as we will discuss in the next section, this is not always the case.

Using this fitting procedure, we have measured the groove angle for several grain boundaries and the results are gathered in Table I. For one grain boundary ( $\Sigma 5$  (100)), the Table also shows the variation of the measurement over time. This measurement was performed on designed grain boundaries, but also on random columnar grain boundaries. In the latter case, we had to search to find a portion of the grain boundary sufficiently straight to allow meaningful averaging of the groove position. It is clear from Table I that the method distinguishes the  $\Sigma 3$  grain boundary, with an angle of  $180^\circ$ , from all the others, which have angles between  $80^\circ$  and  $110^\circ$ . The method is, however, not sufficiently precise to distinguish between the  $\Sigma 5$  and  $\Sigma 17$  grain boundaries. The energies of these two types of grain boundaries have been experimentally measured only for aluminum alloys in [30]. The resulting values were quite similar. A number of numerical simulations have corroborated this measurement [24, 25, 30]. As a consequence, the difference in angle for these boundaries is expected to be small, and our method is not sufficiently precise to distinguish between them.

The grooves observed in this study are typically about  $3 \mu\text{m}$  deep (30 pixels), which corresponds to about three crystal inter-layer distances. This explains why the grooves are difficult to measure precisely and why we had to develop special processing procedures involving averaging over the length of the grain boundary. In the work of Rogers and Ackerson [17], the only other study dealing with this type of grooves in hard-sphere colloidal systems, the depth is about  $10 \mu\text{m}$ . Since their particles are smaller, this corresponds to 30 inter-layer distances. The difference between the two systems (larger particle size, and higher

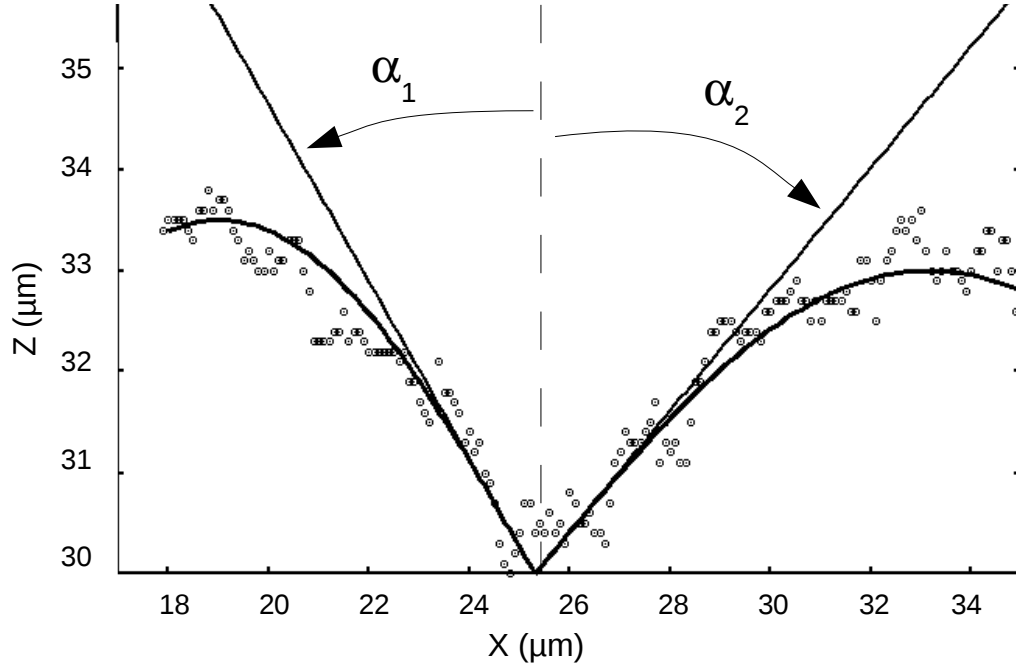


FIG. 10. Fitting of the experimental groove profile.

density mismatch in the present paper) explains the differences between the geometrical characteristics of the grooves. The typical values of the groove angle, however, seem to be similar in both studies.

TABLE I. Measurement of the groove angle,  $\alpha$ , in several grain boundaries.

Grain Boundary type	$\alpha$ ( $^{\circ}$ )
$\Sigma 5$ (100)	85; 104
$\Sigma 5$ (100) over time	106.6; 102.3; 101.7; 105; 109
$\Sigma 17$ (100)	107
$\Sigma 3$ (110)	180
Random columnar	85; 107

## B. Variation of the groove angle with time

We acquired couples of confocal stacks of the  $\Sigma 5$  boundary as described above, but we repeated this measurement over a longer period of time, with approximately 10 minutes between each measurement. We then measured the two contributions to the groove angle ( $\alpha = \alpha_1 + \alpha_2$ ) with the processing method described above. The time-dependence of these two contributions and their geometric average, are plotted in Fig. 11. We observe that over time, the average fluctuates less than the parts. It varies between  $51^\circ$  and  $54^\circ$ , for an  $\alpha$  angle of  $102^\circ$  to  $110^\circ$ . The two contributions separately vary much more (from  $42^\circ$  to  $60^\circ$ ). It appears that the inclination of the grain boundary fluctuates about its average vertical position.

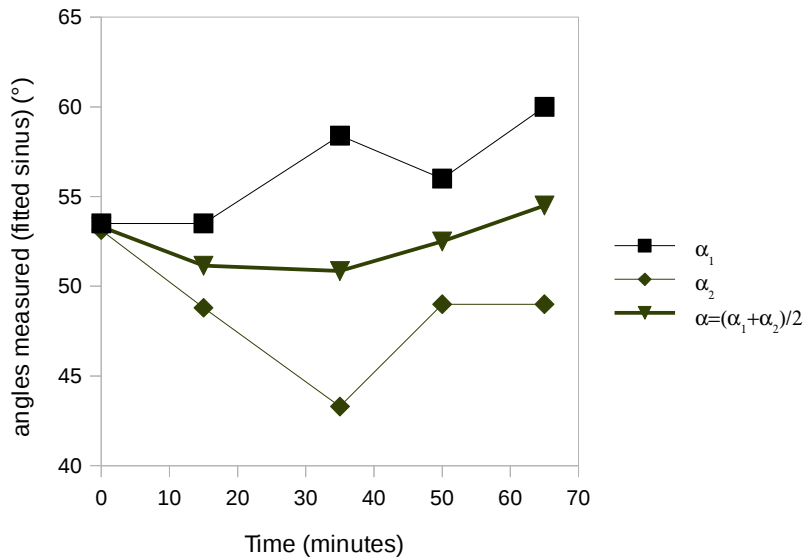


FIG. 11. Time dependence of the two contributions,  $\alpha_1$  and  $\alpha_2$ , to the groove angle  $\alpha$  of the  $\Sigma 5(100)$  boundary. The contributions fluctuate more than the total angle.

### C. Relation between density and mobility

Figure 12 shows a projection of the gray scale density for the same  $\Sigma 5$  (100) grain boundary as the one used for the order parameter shown in Figure 3 and for the mobility map in Figure 6a. This density map was produced by shrinking the thresholded confocal images by a factor of ten, and then resizing the averaged voxels back to the image size of the mobility map. This procedure results in a blurring of the discrete particles, each of which has a diameter of about 15 voxels. The resulting continuum map clearly reveals the liquid and grain boundary regions. In the crystal, away from the boundary, we estimated the packing fraction from the average gray scale to be 61%.

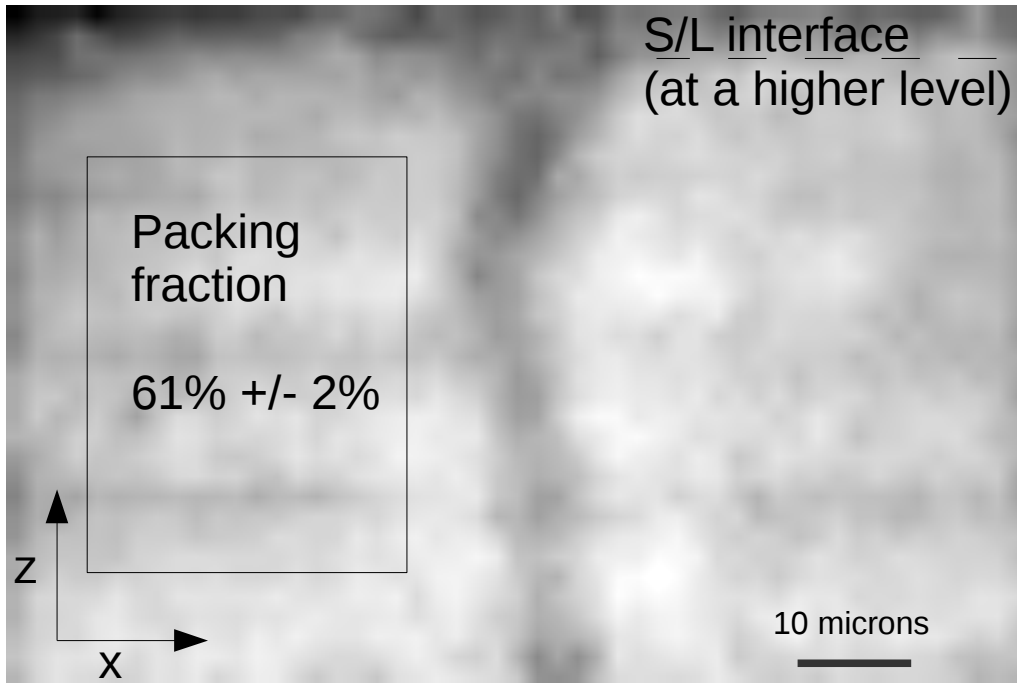


FIG. 12. Average value of the density in the plane perpendicular to the grain boundary (lower densities for darker gray levels). Note that the density is smaller at the grain boundary, at all heights  $Z$ .

The density is lower at the grain boundary and in the liquid (packing fraction of about 30%). The density is fairly constant with the height along the grain boundary. At the triple line, the region with a lower density becomes wider, in good agreement with the shape of

the groove. The mobility shown in Figure 6a is then not directly related to the density, as it is much lower at the bottom of the grain boundary and increases with the height. For a high mobility, it appears from this measurement that the density has to be low, but that this is not a sufficient condition.

Figure 13 is a plot of the local density, computed by projecting the average value of the Voronoi volumes of all the particles in the  $\Sigma 5(100)$  boundary of Figures 3, 6a and 12 onto a plane parallel to the x-z plane. The similarity with Fig. 12 is clear. In the region away from the boundary, the average Voronoi volume of a particle is  $\Omega = 3.37 \mu\text{m}^3$ , which corresponds to a packing fraction of  $\phi = V_p/\Omega = 0.57$ , close to the value measured by the gray-scale method. The Voronoi volume in the perfect crystal with a lattice parameter based on the spacing of the template is  $\Omega_{id} = 3.06 \mu\text{m}^3$ , which corresponds to a packing fraction of 0.63. The difference is due to imperfections (vacancies) in the crystal.

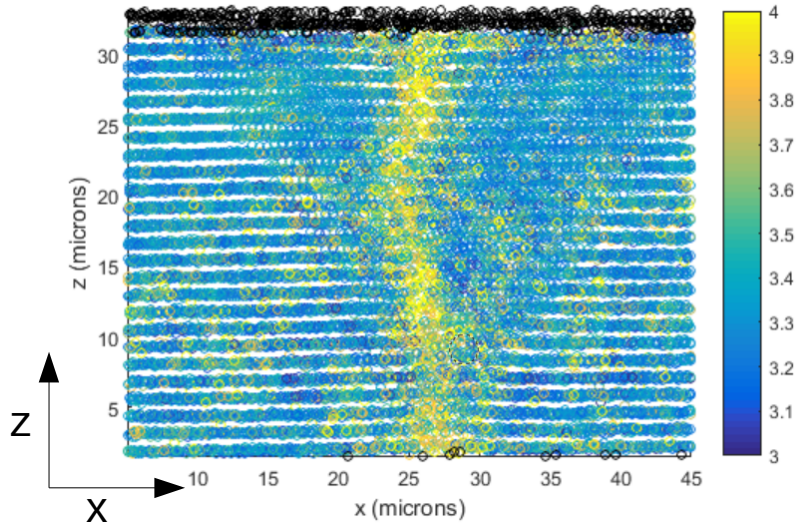


FIG. 13. Average Voronoi volumes of the particles the  $\Sigma 5(100)$  boundary projected onto the x-z plane.

To calculate the density deficit associated with the boundary, a cluster of  $N$  particles that contained a large part of the boundary was considered. A number  $N_{gb}$  of those particles lay at the grain boundary, i.e., they form the end surfaces of the two crystals where they meet at the boundary. If the sum of all the Voronoi volumes of the cluster is  $V$ , the excess

volume is calculated as  $(V - N\Omega)/N_{gb}$ , which here comes to  $V_{ex} = 0.603 \mu\text{m}^3$ . This gives a packing fraction of  $\phi = V_p/(\Omega + V_{ex}) = 0.49$ . We can normalize the excess volume by the average crystalline Voronoi volume:  $V_{ex}/\Omega = 0.17$ . Since there is a bilayer of boundary particles, it is useful to compare twice this value, 0.34, to a similarly normalized value found in the same hard-sphere boundary constructed geometrically, (page 154 of[22]) which gives 0.38.

#### D. Grain Boundary Energy

The energy of a grain boundary can, in principle, be determined from the groove angle from Eq. 2. For example, for the  $\Sigma 5$  (100) boundary, the groove angle is  $105^\circ$  (Fig. 11). This gives for the grain boundary energy  $\gamma_{\Sigma 5}^{exp} = 1.22\gamma_{SL}$ . Computer simulations [31] and colloid experiments [3] show that the solid-liquid interfacial energy in the hard-sphere system is only slightly anisotropic, and has an average value  $\gamma_{SL} \approx 0.6 k_B T \sigma^{-2}$ . This gives an experimental estimate of the grain boundary energy  $\gamma_{\Sigma 5}^{exp} \approx 0.73 k_B T \sigma^{-2}$ .

It is interesting to compare this value to a simple theoretical estimate of the free energy of formation of the grain boundary. The equation of state of the hard-sphere system [32–34] gives a pressure at solid-liquid equilibrium  $p = 11.5 k_B T / \Omega$ . To increase the volume at the boundary by  $2V_{ex} = 0.34\Omega$  per particle in the boundary plane requires work equal to  $\Delta H = p 2V_{ex} = 0.34 \times 11.5 k_B T = 3.9 k_B T$ . The increase in volume also leads to an increase in entropy, which, for one each of the grain boundary particles, can be estimated from the change in free volume as  $\Delta S = k_B \ln [(\Omega + V_{ex} - \Omega_0) / (\Omega - \Omega_0)]$ , where  $\Omega_0 = \sqrt{2}/2 \sigma^3$  is the volume per particle at maximum close packing. This gives  $\Delta S = 0.49 k_B$ .

The resulting increase in free energy, per particle in the boundary plane is  $\Delta G = \Delta H - 2T\Delta S = 3 k_B T$ , where the factor of two in the entropy arises from there being a bilayer of boundary particles. Since the boundary is along a (210) plane, the area per particle in that plane is  $\Omega/d_{210} = 1.519 \sigma^2$ , where  $d_{210} = \frac{\pi}{6} \sqrt{\frac{5}{2}} \frac{\sigma^2}{\phi}$  is the plane spacing in the crystal, and the packing fraction  $\phi = 0.545$  near the solid-liquid interface is used [19, 33]. The grain boundary energy then becomes  $\gamma_{\Sigma 5}^{th} = 1.9 k_B T \sigma^{-2} = 2.6 \gamma_{\Sigma 5}^{exp}$ . The large difference between the two values probably means that there are substantial entropy contributions which have not been taken into account.

## VI. CONCLUSION

In this paper we have studied the structure of model grain boundaries in colloidal crystals. We have used a new observation method based on the consecutive acquisition of two images of the same grain boundary. The differences between these images can be used to reveal the regions where the particle mobility is high. The mobility was high at the grain boundary and increased with the height. Projecting this mobility onto a plane perpendicular to the grain boundary revealed the presence of grooves at the grain boundary / liquid triple line. Grooves were observed for all boundaries, except for the zero-energy  $\Sigma 3$  (110) twin boundary. Measuring the angle at these grooves over time for a same grain boundary showed that the grooves can be non symmetric but that the angle fluctuation is relatively small. The measurement of the angle was shown to be sensitive to the threshold on the mobility selected for separating the liquid and the solid. The values leading to the least noisy profiles corresponded to a liquid/solid interface located at an altitude where the mobility is very high but where the structure of the atoms still looks like this of a crystal. The value of the groove angles indicate that there is a substantial local entropy increase near the boundary.

## ACKNOWLEDGMENTS

We thank Tom Kodger and Katherine Jensen for their help in fabricating the samples. This work was carried out during a sabbatical leave of Eric Maire at Harvard University, sponsored by the French CNRS and was supported by the National Science Foundation by contract N° DMR-1206765.

- 
- [1] U. Gasser, E.R. Weeks, A. Schofield, P.N. Pusey, and D.A. Weitz. Real-space imaging of nucleation and growth in colloidal crystallization. *Science*, 292(5515):258–262, 2001.
  - [2] Z.R. Wang, F. Wang, Y; Peng, Z;Y. Zheng, and Y;L. Han. Imaging the homogeneous nucleation during the melting of superheated colloidal crystals. *Science*, 338(6103):87–90, 2012.
  - [3] I.B. Ramsteiner, D.A. Weitz, and F. Spaepen. Stiffness of the crystal-liquid interface in a hard-sphere colloidal system measured from capillary fluctuations. *Physical review. E*, 82(4):041603, 2010.

- [4] P. Schall, I. Cohen, D.A. Weitz, and F. Spaepen. Visualization of dislocation dynamics in colloidal crystals. *Science*, 305(5692):1944–1948, SEP 24 2004.
- [5] P. Schall, I. Cohen, D.A. Weitz, and F. Spaepen. Visualizing dislocation nucleation by indenting colloidal crystals. *Nature*, 440(7082):319–323, 2006.
- [6] P. Schall, D.A. Weitz, and F. Spaepen. Structural rearrangements that govern flow in colloidal glasses. *Science*, 318(5858):1895–1899, 2007.
- [7] K.E. Jensen, D.A. Weitz, and F. Spaepen. Local shear transformations in deformed and quiescent hard-sphere colloidal glasses. *Physical Review E*, 90(4):042305, 2014.
- [8] A.P. Sutton and R.W. Balluffi. *Interfaces in Crystalline Materials*. Oxford, 1995.
- [9] J.M. Howe. *Interfaces in materials*. Wiley, 1997.
- [10] T.O.E. Skinner, D.G.A.L. Aarts, and R.P.A. Dullens. Grain-boundary fluctuations in two-dimensional colloidal crystals. *Physical Review Letters*, 105:168301, 2010.
- [11] K.H. Nagamanasa, S. Gokhale, R. Ganapathy, and A.K. Sood. Confined glassy dynamics at grain boundaries in colloidal crystals. *Proceedings of the National Academy of Sciences of the United States of America*, 108(28):11323–11326, 2011.
- [12] S. Gokhale, K.H. Nagamanasa, V. Santhosh, A.K. Sood, and R. Ganapathy. Directional grain growth from anisotropic kinetic roughening of grain boundaries in sheared colloidal crystals. *Proceedings of the National Academy of Sciences of the United States of America*, 109(50):20314–20319, 2012.
- [13] A. M. Alsayed, M. F. Islam, J. Zhang, P. J. Collings, and A. G. Yodh. Premelting at defects within bulk colloidal crystals. *Science*, 309(5738):1207–1210, 2005.
- [14] E. Maire, M. Gulda Persson, N. Nakamura, K.E. Jensen, E. Margolis, C. Friedsam, and F. Spaepen. Three dimensional confocal microscopy study of boundaries between colloidal crystals. In *Optical Measurements, Modeling, and Metrology, Volume 5*, pages 69–74. Springer, 2011.
- [15] C Herring. chapter 8 in the physics of powder metallurgy, edited by we kingston. McGraw-Hill Book Co., New York, 1951.
- [16] C. Herring. The use of classical macroscopic concepts in surface energy problems. In *Structure and properties of solid surfaces*, page 5. U. Chicago press, 1953.
- [17] R.B. Rogers and B.J. Ackerson. The measurement of solid-liquid interfacial energy in colloidal suspensions using grain boundary grooves. *Philosophical Magazine*, 91(5):682–729, 2011.

- [18] M.E. Glicksman and C.L. Vold. Determination of absolute solid-liquid interfacial free energies in metals. *Acta Metallurgica*, 17(1):1–11, 1969.
- [19] K.E. Jensen, D. Pennachio, D. Recht, D.A. Weitz, and F. Spaepen. Rapid growth of large, defect-free colloidal crystals. *Soft Matter*, 9(1):320–328, 2013.
- [20] H.J. Frost, F. Spaepen, and M.F. Ashby. A second report on tilt boundaries in hard sphere f.c.c. crystals. *Scripta Metallurgica*, 16(10):1165 – 1170, 1982.
- [21] H.J. Frost, M.F. Ashby, and F. Spaepen. A first report on a systematic study of tilt-boundaries in hard-sphere f.c.c. crystals. *Scripta Metallurgica*, 14(10):1051 – 1056, 1980.
- [22] H.J. Frost, M.F. Ashby, and F.A. Spaepen. A catalogue of [100], [110], and [111] symmetric tilt boundaries in face-centered cubic hard sphere crystals. *Harvard University - <http://nrs.harvard.edu/urn-3:HUL.InstRepos:13851353>*, 1982.
- [23] G.C. Hasson and C. Goux. Interfacial energies of tilt boundaries in aluminium. experimental and theoretical determination. *Scripta Metallurgica*, 5(10):889 – 894, 1971.
- [24] E.A. Holm, G.S. Rohrer, S.M. Foiles, A.D. Rollett, H.M. Miller, and D.L. Olmsted. Validating computed grain boundary energies in fcc metals using the grain boundary character distribution. *Acta Materialia*, 59(13):5250 – 5256, 2011.
- [25] G.S. Rohrer, E.A. Holm, A.D. Rollett, S.M. Foiles, J. Li, and D.L. Olmsted. Comparing calculated and measured grain boundary energies in nickel. *Acta Materialia*, 58(15):5063 – 5069, 2010.
- [26] P.J. Lu, P.A. Sims, H. Oki, J.B. Macarthur, and D.A. Weitz. Target-locking acquisition with real-time confocal (tarc) microscopy. *Optics Express*, 15(14):8702–8712, 2007.
- [27] Y. Gao and M.L. Kilfoil. Accurate detection and complete tracking of large populations of features in three dimensions. *Optics Express*, 17:4685, 2009.
- [28] K.E. Jensen and N. Nakamura. An iterative algorithm to improve colloidal particle locating. *arXiv preprint [arXiv:1508.04695](https://arxiv.org/abs/1508.04695)*, 2015.
- [29] G. Ackland and A. Jones. Applications of local crystal structure measures in experiment and simulation. *Phys. Rev. B*, 73:054104, 2006.
- [30] G. Hasson, J.-Y. Boos, I. Herbeuval, M. Biscondi, and C. Goux. Theoretical and experimental determinations of grain boundary structures and energies: Correlation with various experimental results. *Surface Science*, 31(0):115 – 137, 1972.

- [31] Ruslan L Davidchack, James R Morris, and Brian B Laird. The anisotropic hard-sphere crystal-melt interfacial free energy from fluctuations. *The Journal of chemical physics*, 125(9):094710, 2006.
- [32] B.J. Alder, W.G. Hoover, and D.A. Young. Studies in molecular dynamics. v. high-density equation of state and entropy for hard disks and spheres. *The Journal of Chemical Physics*, 49(8):3688–3696, 1968.
- [33] K.R. Hall. Another hard-sphere equation of state. *The Journal of Chemical Physics*, 57(6):2252–2254, 1972.
- [34] N.F. Carnahan and K.E. Starling. Equation of state for nonattracting rigid spheres. *The Journal of Chemical Physics*, 51(2):635–636, 1969.